InAs Colloidal Quantum Dot Photodiode Stack for CMOS-Integrated Infrared Imaging

Abu Bakar Siddik[1,2], Wenya Song[1], Epimitheas Georgitzikis[1*], Marina Vildanova[1], Minhyun Jin[1], Francois Berghmans[1], Itai Lieberman[1], Pawel E. Malinowski[1], Thierry Conard[1], David Cheyns[1] and Paul Heremans[1,2].*

[1]IMEC, Kapeldreef 75, 3001 Leuven, Belgium.

[2]Dept. of Electrical Engineering ESAT, KU Leuven, Kasteelpark Arenberg 10, 3001 Leuven, Belgium.

KEYWORDS

InAs colloidal quantum dot, IGZO, CuI, cryogenic J−V and C−V, traps, photoelectron spectroscopy, CMOS-integrated infrared imager

ABSTRACT

Heavy-metal-free III–V semiconductor-based colloidal quantum dots (CQDs), such as InAs, are promising candidates for near- and short-wave infrared detection. However, up-to-date research efforts remain mainly limited to wavelengths below 1100 nm due to challenges in synthesis, junction formation and passivation for large diameter InAs quantum dots. Systematic investigations into device design, reverse dark current mechanisms, and trap distributions in larger InAs quantum dots remain limited. Here, we report a thin-film PIN heterojunction colloidal InAs

(1200 nm) photodiode stack with amorphous indium gallium zinc oxide and Copper(I) Iodide transport layers. To the best of our knowledge, the device exhibits one of the lowest reported dark current densities of 4.7 μA/cm² at −1 V and 298 K, which decreases to 3.6 nA/cm² at 220 K. Temperature-dependent current-voltage characteristics and activation energy analysis confirm thermally driven dark current increasing with applied field. Impedance spectroscopy reveals the dominant deep trap states within the InAs CQD layer, being tail states of the conduction band that reach down to ~0.4 eV below the band edge, with a density of ~2×10^{16} cm^{-3}. The temperature-induced increase in carrier density and reduction in built-in potential within the depleted InAs layer reflect trap filling and Fermi level pinning in the N and P layers. The trapping-detrapping induced noise reduces the specific detectivity (D*) at −1 V by 1.97 orders at 1 Hz and by 1.52 orders of magnitude at 10 Hz relative to the shot-noise-limited baseline. At frequencies ~≥500 Hz the D* approaches the calculated limit of 2.5×10^{11} Jones. Finally, we demonstrate infrared imaging by monolithically integrating the photodiode with a Si read-out IC, enabling imaging beyond the spectral range of CMOS sensors.

1. INTRODUCTION

Infrared photodetectors have attracted growing interest due to their broad application in imaging, sensing, and communication [1–3]. Epitaxial III–V semiconductors offer excellent performance, but their high cost and limited scalability due to flip-chip hybridization remain limiting factors[1,3]. Although progress in Cu–Cu bonding is promising for improved integration, achieving pixel pitches comparable to what can be reached by CMOS image sensors remains a significant challenge [4,5]. Colloidal quantum dots (CQDs), with their solution processability, bandgap tunability, and compatibility with CMOS integration, present a promising platform for cost-

effective infrared photodetectors [2,6–8]. In particular, III–V InAs CQDs offer the potential to extend detection into the short-wave infrared (SWIR) range without relying on toxic heavy metals [6,9–12].

Recent progress in InAs CQD synthesis, surface passivation, and device design has led to improved device metrics such as external quantum efficiency (EQE) and detectivity [6,10,13,14]. Strategies including co-passivation, surface ligand exchange, and doping have addressed some of the inherent challenges posed by the covalent InAs surface, enabling improved charge transport and reduced trap-mediated recombination [11,14,15]. However, most of the reported work remains focused on absorption wavelengths below ~1100 nm, as increasing quantum dot size to extend the absorption further into the SWIR introduces new complications [12]. Larger InAs CQDs exhibit increased trap densities, challenges in achieving proper rectification, and difficulties in forming efficient junctions due to band-edge shifts and limited energy level alignment with conventional transport layers [12,14].

Unlike most thin-film colloidal quantum dot photodiodes (QDPDs) reported in the literature, which are fabricated on ITO/glass substrates [6,12,13,16,17], we optimized the device stack directly on a Si substrate using CMOS-compatible TiN as the top electrode. Because of back-end-of-line (BEOL) compatibility, we utilized amorphous indium gallium zinc oxide (a-IGZO), which, as demonstrated in our previous work, can serve dual roles as both electron transport layer (ETL) and transfer gate for advanced thin-film pinned photodiode structures [18]. As the InAs CQD bandgap narrows, the entire band structure shifts downward, complicating energetic alignment with the valence band maximum (VBM) of conventional hole transport layers (HTLs) [12,14]. Although MoOx, with its deeper HOMO level, has been widely adopted as a hole-selective recombination layer in InAs CQD devices, it often leads to poor rectification and elevated dark current densities [12,14]. We introduce Copper(I) Iodide (CuI), possessing a deeper VBM, as the HTL to form a CuI–

InAs CQD–IGZO PIN heterojunction that promotes efficient carrier separation and full depletion [19,20].

The optimized device achieves a dark current density of 4.7 μA/cm² at –1 V with an external quantum efficiency (EQE) of 25% at 1210 nm. Temperature-dependent current-voltage (J–V) analysis indicates that thermal generation through trap states within the CQD layer dominates the dark current. As the CQD size increases, surface passivation becomes increasingly challenging, leading to higher trap densities that directly impact device performance. We therefore quantify trap states via impedance spectroscopy and correlate their energetic position with band structure derived from ultraviolet photoelectron spectroscopy (UPS). While numerous studies have focused on synthesis and device optimization of InAs infrared CQDs[14,21–23], demonstrations of practical imaging applications remain limited. Here, we further demonstrate the monolithic integration of the InAs CQD photodiode with the Si ROIC, validating its infrared imaging capability.

2. RESULTS AND DISCUSSION

2.1 Device design and characterization

The complete InAs QDPD stack on Si consists of TiN, IGZO, $InBr_3$ treated InAs CQD, CuI, poly[4,8-bis(5-(2-ethylhexyl)thiophen-2-yl)benzo[1,2b;4,5-b′]dithiophene-2,6-diyl-alt-(4-(2-ethylhexyl)-3fluorothieno[3,4-b]thiophene-)-2-carboxylate-2-6-diyl)] (PTB7-Th), MoOx and ITO as shown in the schematic and transmission electron microscopy (TEM) cross-section in Figure 1a-b, respectively. The detailed fabrication flow of the photodiode and imager chip is included in the experimental section. We utilize InAs CQDs with an excitonic peak at 1200 nm, prepared by solution-phase $InBr_3$ ligand exchange following the method (Figure S2) introduced by Sargent et

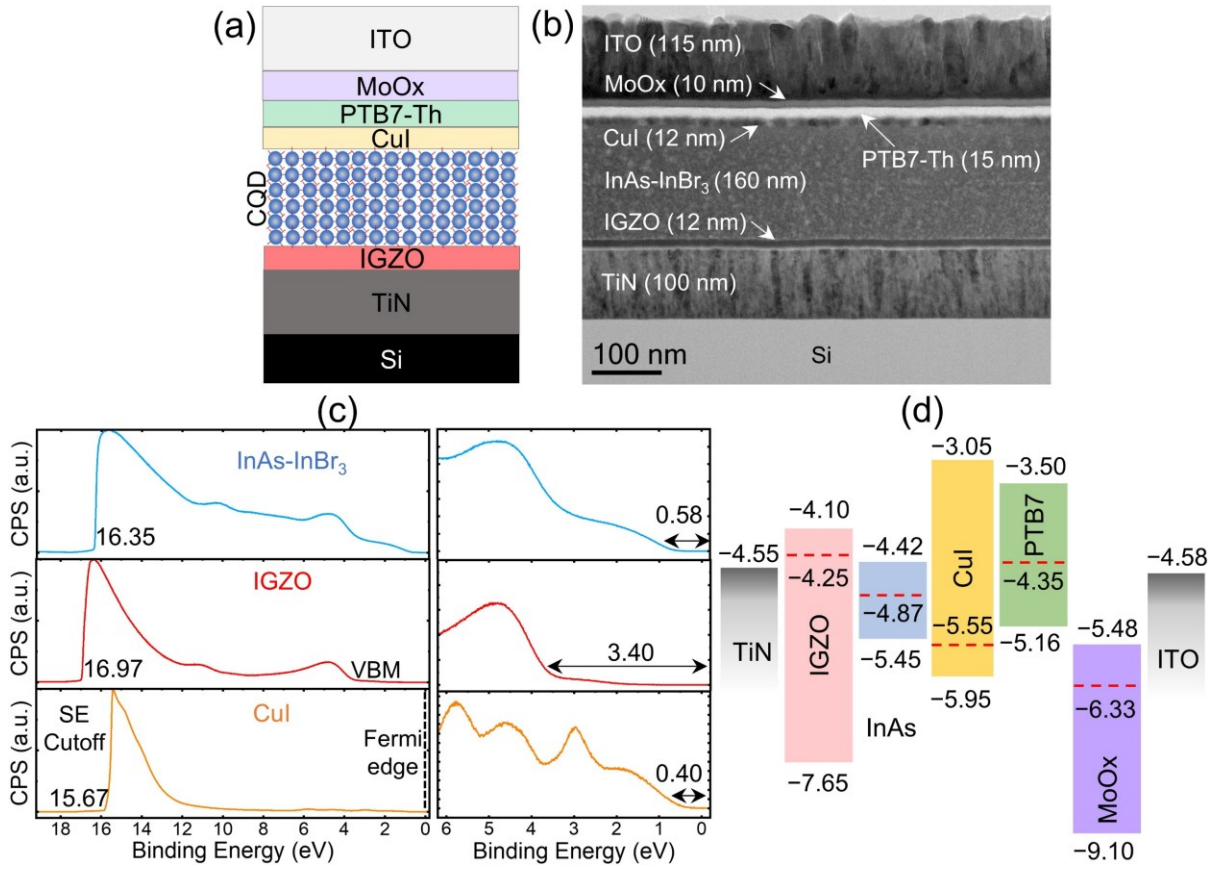


Figure 1. (a) Schematic and (b) TEM cross-section of the InAs CQD photodiode. (c) Full UPS spectra of InAs−$InBr_3$, IGZO and CuI showing secondary electron (SE) cutoff, valence, and Fermi edges. (d) The vacuum referenced energy band diagram of the full thin film stack.

al. [6,12]. The physical dimension range of the CQD (~4.4−4.7 nm) from TEM, along with the absorption spectra before and after ligand exchange are included in Figure S1a-b. Figure 1c shows the ultraviolet photoelectron spectroscopy (UPS) spectra of InAs-$InBr_3$, IGZO and CuI showing secondary electron (SE) cutoff, VBM edge and Fermi edge. Using the extracted ionization energies (IE) and work functions (WF) from the measured UPS spectra (InAs-$InBr_3$, IGZO and CuI) in Figure 1c, together with energy level values for TiN, PTB7-Th, MoOx, and ITO taken from our previous work [24], we constructed a vacuum-referenced (0 eV) energy band diagram of the full stack, shown in Figure 1d. In line with recent reports [6,7,13,25] the larger InAs CQDs treated with

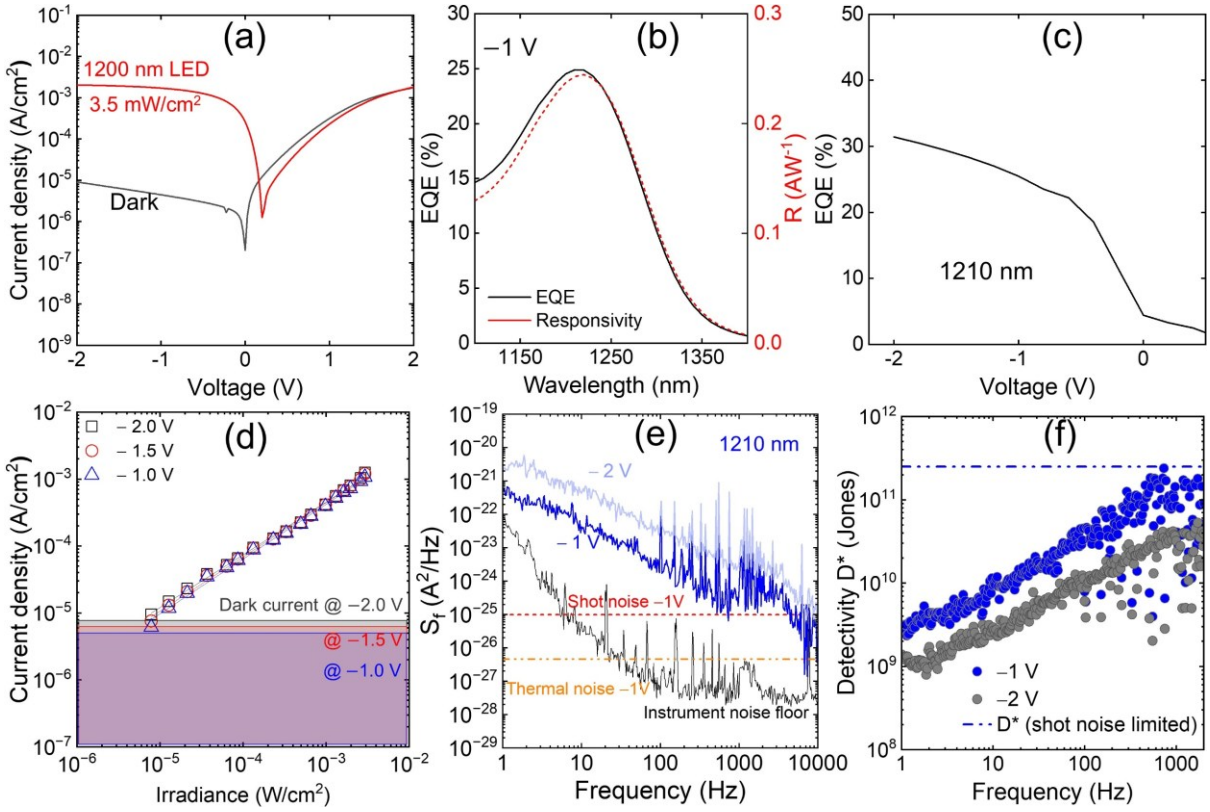


Figure 2. (a) Dark and IR light illuminated (1200 nm) J−V characteristics, (b) EQE and responsivity at reveres bias −1 V, and (c) EQE as a function of reverse bias voltages at wavelength 1210 nm. (d) Linearity of J−V characteristics under different light power at various reverse biases. (e) Measured room temperature noise power spectral density S_f (A^2/Hz) at −1 and −2 V (blue), calculated shot (red) and thermal (orange) noise limits at −1 V and instrument noise floor (black). (f) Frequency dependent specific detectivity (D*) at −1 and −2 V and calculated shot noise limited specific detectivity at −1 V.

$InBr_3$ exhibit a downward shift of the overall band structure (measured ionization energy for 1200 nm InAs-$InBr_3$: ~5.45 eV) resulting in inefficient hole transport due to misalignment with VBM of HTL. Therefore MoOx, with its deeper electron affinity (EA) level (measured MoOx EA ~5.48 eV [24]), has been widely adopted as a hole-selective recombination layer in InAs CQD devices, however, it often leads to poor rectification and elevated dark current densities. Here, we introduce CuI as HTL layer with a deeper IE of ~5.95 eV that aligns well with InAs-$InBr_3$ active layer VBM for hole extraction. Details of the efficient hole extraction barrier are discussed later based on the Fermi-referenced energy band diagram (Figure 5a). Thanks to the large work function separation

~1.3 eV (maximum theoretical limit for built-in potential) between CuI (~5.55 eV) and IGZO (~4.25 eV), this pair of transport layers ensures full depletion across the lightly n-doped (from VBM and WF separation) InAs-$InBr_3$ absorber layer. However, due to polycrystalline growth of CuI and the presence of large grain boundaries, as can be seen in Figure S3, we introduce a thin layer (~13 nm) of PTB7-Th to ensure continuity of the hole transport layers. Furthermore, MoOx on top of PTB7-Th protects the polymer from sputtering damage and ensures good contact with ITO. A complete elemental mapping (EDS) and depth profile of the full device are presented in Figure S4−5, to highlight the sharp interfaces achieved between all the layers.

The J−V characteristics of the InAs QDPD under dark and infrared LED illumination (1200 nm ~3.5 mW/cm^2) shown in Figure 2a exhibit a photocurrent-to-dark current ratio of ~2.6 orders of magnitude at −1 V. The photocurrent response suggests that the InAs−$InBr_3$ is partially depleted at equilibrium and achieves full depletion at reverse bias beyond 0.5 V, therefore all the extracted data throughout the manuscript are reported for −1 V or more negative. Figure 2b-c present measured EQE and responsivity as a function of wavelength at −1 V, and EQE vs reverse bias voltage at 1210 nm, respectively. Reverse-biased photocurrent density under various illumination powers (Figure 2d) shows good linearity. Although it is common to calculate detectivity assuming the device is shot-noise-limited, Fang et.al. and several other reports [26–28] emphasize the importance of noise characterization, highlighting that the specific detectivity (D*) can easily be overestimated by assuming shot-noise limited operation. Here, we carefully measure the noise power spectral density (Figure 2e) of the InAs QDPD at −1 and −2 V, along with estimated shot and thermal noise, and the instrument noise floor. The noise power spectral density (S_f) of the device is strongly frequency-dependent below 500 Hz, where it exceeds the calculated shot noise limit, especially at ≤10 Hz. The shot-noise-based estimation becomes valid above ~500 Hz, where

the measured noise approaches the shot noise limit. The D* based on measured noise and estimated shot-noise-limited value is plotted in Figure 2f. The noise limited D* at −1 V is overestimated by 1.97 orders at 1 Hz and 1.52 orders of magnitude at 10 Hz, and it approaches the calculated shot-noise-limited D* of 2.5×10^{11} Jones at frequencies ≥500 Hz. The J–V characteristics from 10 devices measured across a single substrate, as well as the device's air stability are shown in Figure S6a–b, respectively. The normalized transient photo response of the InAs QDPD with a large device area of 0.0625 cm² is summarized in Figure S7. To contextualize the performance of our device, Table 1 compares key metrics with state-of-the-art InAs photodetectors reported in recent literature. Most state-of-the-art CQD photodiodes are demonstrated on ITO/glass substrates, which, while effective for benchmarking, do not directly translate to CMOS-compatible silicon platforms. In contrast, our approach starts from a Si substrate with CMOS backend metallization, offering a practical path toward scalable monolithic integration.

Table 1. Comparison of Performance Metrics for State-of-the-Art InAs QDPDs at −1 V

Substrate	λ (nm)	EQE (%)	J_D (A/cm²)	R (A/W)	D* (Jones)	Application Demonstration	Reference
glass/ITO	940	47	$\sim5\times10^{-6}$	~ 0.6	3.10×10^{11}	–	Shin et al.[9]
glass/ITO	970	53	$\sim2\times10^{-7}$	~0.42	6.90×10^{11}	–	Xia et al.[17]
glass/ITO	1020	43.1	$\sim2\times10^{-7}$	~ 0.36	1.40×10^{12}	–	Jung et al.[10]
glass/ITO	1050	–	$\sim1\times10^{-5}$	~ 0.4	2.98×10^{8}	–	Kim et al.[13]
glass/ITO	1120	35	$\sim4\times10^{-7}$	~0.36	8.80×10^{11}	–	Vafaie et al.[12]
glass/ITO	1140	75	$\sim2\times10^{-7}$	–	5.00×10^{11}	–	Xia et al.[16]
glass/ITO	1200	~7	$\sim4\times10^{-7}$	~0.067	–	–	Vafaie et al.[12]
glass/ITO	1240	2.7	$\sim7\times10^{-5}$	~ 0.027	5.70×10^{9}	–	Leemans et al.[2]
Si	1210	25	$\sim4\times10^{-6}$	~0.25	2.50×10^{11} (>500 Hz)	Imager on Si ROIC	This work

2.2 Temperature-Dependent Insights into Dark Reverse-Biased Carrier Dynamics

Although we achieve one of the lowest reported dark current densities (~4.7 μA/cm²) in InAs QDPDs absorbing at 1200 nm, it remains important to investigate the origin of the reverse dark current to better understand the device carrier dynamics and further optimize device performance. To this end, we first characterize the dark quasi-static J−V curves in the temperature range from 220 K to 350 K, see Figure 3a. Cooling to 220 K reduces the dark current density to 3.6 nA/cm², while heating to 350 K increases it to 215 μA/cm², revealing the thermally activated nature of the dark current. Using the Arrhenius plots (Figure 3b) at increasing applied reverse fields and their respective fittings, we extracted and plotted the activation energies in Figure 3c. The extracted activation energies (E_A) of 0.57 eV at low bias (−0.25 V) suggest that thermally activated carrier generation is dominated by deep trap states, likely located near the mid-gap. The observed reduction in E_A with increasing reverse bias (0.49 eV at −2 V) is attributed to field-assisted trap emission processes, consistent with Poole–Frenkel-like barrier lowering as we discussed in our previous work [24]. The Poole–Frenkel plot in Figure S8a shows increasing linearity of ln(J/E) vs $\sqrt{E}$ as temperature decreases to 220 K from 298 K, indicating that field-enhanced emission becomes more prominent as thermal emission is suppressed. Further cooling down to 77 K lowers the dark current at −1 V to 185 pA/cm² (Figure S8b), consistent with thermally activated trap-limited behavior in the InAs CQD layer.

Given the thermally activated nature of carrier generation, temperature is expected to impact the built-in potential (V_{bi}) and carrier density, as trap occupancy and de-trapping processes can modify

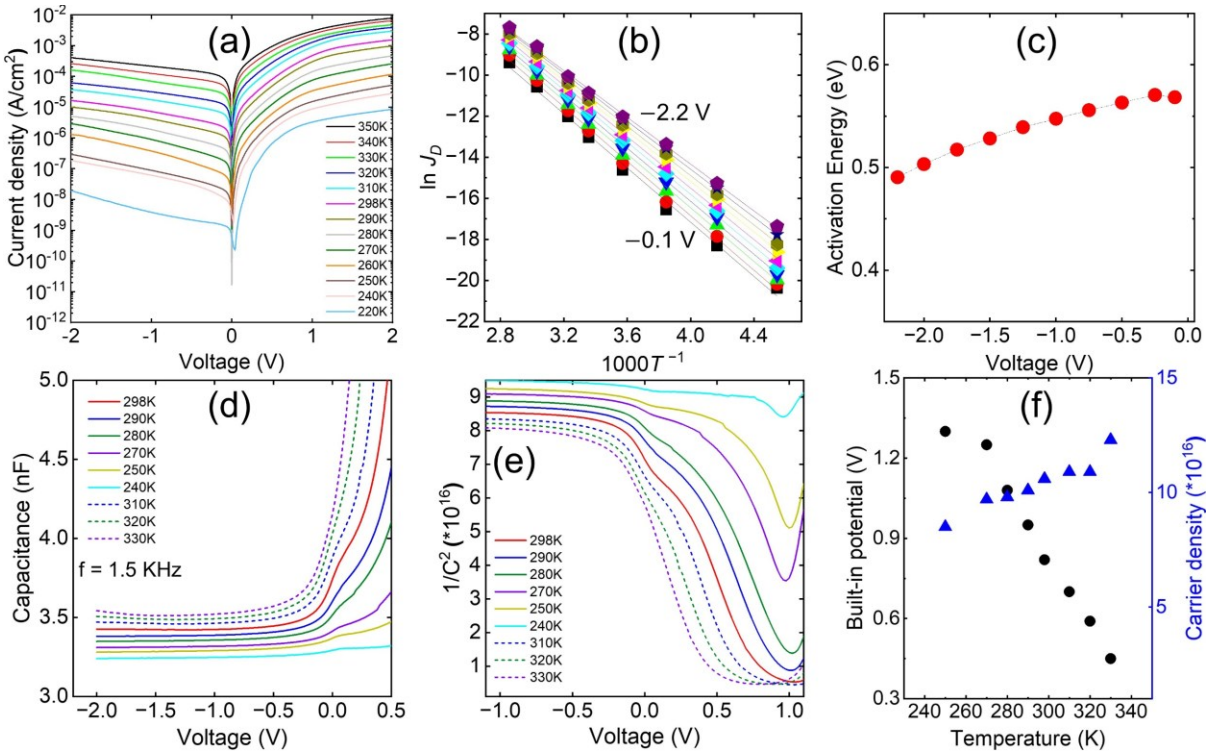


Figure 3. Temperature dependent (350 K−220 K) J-V characteristics, respective Arrhenius plots and extracted activation energies at different reverse bias voltages (a)-(c). Temperature dependent capacitance−voltage characteristics measured at 1.5 KHz, Mott−Schottky plots ($1/C^2$) of the respective C−V curves and extracted build-in-potential and carrier density as a function of temperature are in (d-f), respectively.

the space charge distribution. Capacitance−voltage ($C-V$) measurements are performed at cryogenic and elevated temperatures above 298 K at 1.5 KHz, to enable Mott–Schottky analysis (Figures 3d-e). The Mott-Schottky linear fitting yields a room-temperature V_{bi} of 0.82 V and carrier density of 1.06×10^{17} cm^{-3}. With increasing temperature, the carrier concentration rises to 1.23×10^{17} cm^{-3} at 330 K, likely thermally activated trap filling. As the device is cooled to 250 K, the carrier concentration decreases to 8.50×10^{16} cm^{-3} consistent with trap freeze-out behavior. The extracted V_{bi} shows a similar trend consistent with the change in carrier concentration as higher free carrier density leads to narrower depletion width, a reduced potential drop across the junction, and potential Fermi pinning [29–32].

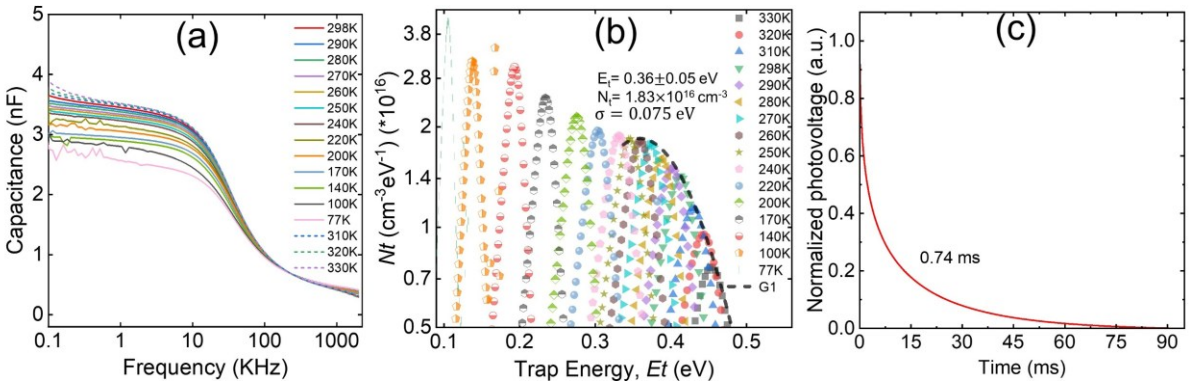


Figure 4. (a) Frequency-dependent capacitance spectra at different temperatures. (b) Trap density and energy at different temperatures and their gaussian fits to extract distribution of shallow and deep trap states. (c) Normalized transient photovoltage decay of the InAs QDPD.

To comprehensively quantify trap states we measured capacitance–frequency ($C-f$) spectra from 330 K to 77 K, spanning both above-ambient and cryogenic conditions. The results are shown in Figure 4a. The measured capacitance values are corrected by subtracting the geometric capacitance (Figure S9), estimated from the high-frequency plateau. The trap density (N_t (E)) and distribution (E_t) are reconstructed from $C-f$ spectra via impedance spectroscopy, using the differential capacitance method originally proposed by Walter et al. [33] and further discussed by Kublitski et al. [34]. The method is briefly discussed in Supplementary Note including the N_t (E) and E_t equations. The resulting N_t (E) spectra are reconstructed individually for each temperature based on the temperature-dependent E_t as shown in Figure 4b. A tail of shallow states, at the level of $2-3\times10^{16}$ cm^{-3}, is observed below the conduction band edge, extending across a broad energy range and terminating in a Gaussian-like function of deep traps. The Gaussian fit yielded a deep trap centered at $0.36\pm0.05\ eV$ below the conduction band, with $N_t = 1.83\times10^{16}$ $cm^{-3}eV^{-1}$ and $\sigma =$ 0.075 eV. Sun et al.[32] reported that the charge-imbalanced nature of the InAs CQD surface leads to poor passivation and high density of surface states primarily originating from In and As dangling bonds. Xia et al.[16] emphasized the presence of deep traps arising from surface defects even after

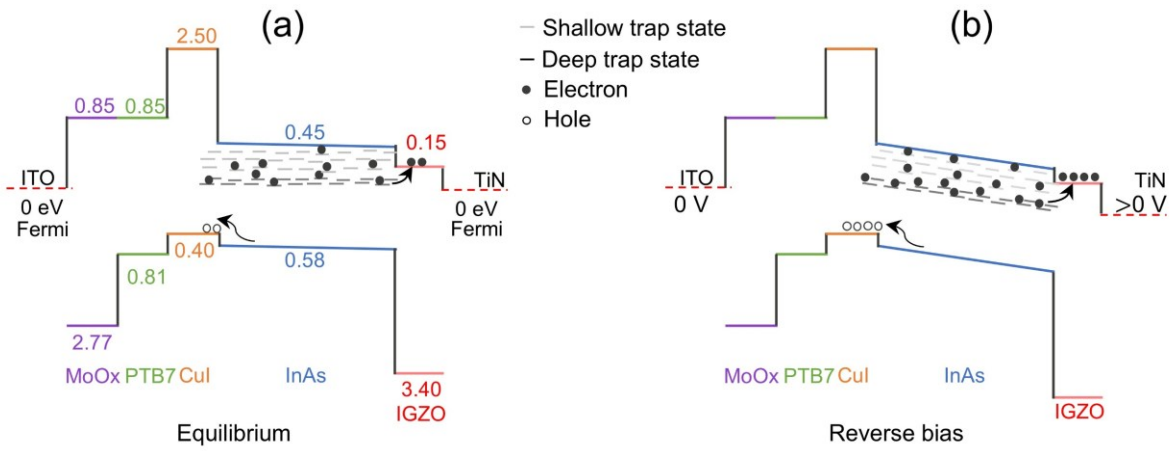


Figure 5. Carrier dynamics illustrated through Fermi-level-referenced (0 eV) energy band diagrams under (a) equilibrium condition and (b) applied reverse bias. Energetically distributed trap states extracted from impedance spectroscopy are included to show their influence on charge transport.

halide passivation, reporting a trap density of 3.20×10^{16} cm^{-3} for Br-passivated InAs CQDs. They further showed that mixed halide ligands can reduce trap densities, achieving 5×10^{15} cm^{-3}, and noted that reactive surface dangling bonds can interact with oxygen and moisture to form oxides and defect states which are consistent with the oxidation features we observe in the As3d binding energy (Figure S10). The presence of distributed traps suggests a charge trapping limited conduction mechanism, which can impact carrier extraction and contribute to the noise power spectral density [34]. Transient photovoltage decay (Figure 4c) under pulsed illumination shows a bi-exponential profile (Figure S11) with lifetimes of 68 μs and 1.15 ms, and a weighted average of 0.74 ms. The fast and slow components likely reflect recombination via shallow and deep traps, respectively, consistent with the trap distributions extracted from *C–f* analysis. In addition, the mobility and trap density of the InAs-$InBr_3$ CQD layer are evaluated by fabricating an electron-only TiN/InAs CQD/Au junction (Figure S12–S13), using the space-charge-limited current (SCLC) method described by Kim et al. [35] and Kim et al. [36]. An electron mobility of 8.72×10^{-4} $cm^2V^{-1}s^{-1}$ is extracted, consistent with the value reported by Song et al. [7] for Br-treated InAs CQDs. These

findings confirm that poor surface passivation leads to a high density of active trap states, which fundamentally limits charge transport in the InAs CQD layer. Furthermore, the calculated trap density of ~ 5.94×10^{15} cm^{-3} obtained from the SCLC fitting (Figure S13), aligns well with the value independently extracted from impedance spectroscopy, reinforcing the reliability of the observed trap-limited transport behavior.

We combine UPS-derived energy band structures and impedance spectroscopy-based trap quantification to visualize the dark carrier dynamics in the complete thin-film InAs photodiode stack (Figure 5). Since the $C-f$ response primarily originates from the depletion region, and the device is fully depleted at -1 V with the geometric capacitance subtracted, we attribute the extracted trap distribution predominantly to the InAs CQD layer. The Fermi (0 eV) energy referenced band diagram (Figure 5a) at thermodynamic equilibrium suggests that the thermally generated carriers (electrons) under dark conditions can easily be emitted to IGZO layer. The presence of both shallow and deep traps in the InAs CQD layer enables thermally assisted transitions via multiple energy states, facilitating carrier excitation into the conduction band. Holes generated in this process can traverse through the CuI valence band, pass through the PTB7-Th layer, and eventually reach the MoOx layer where they are likely to recombine. Under applied reverse bias conditions (Figure 5b), thermal carrier generation is further enhanced, consistent with the trends observed in the field-dependent activation energy analysis.

2.3 Imager chip: Monolithically integrated InAs QDPD on Si ROIC

To demonstrate the imaging capabilities of our InAs QDPD technology, we integrate a pixelated photodiode array onto a CMOS read-out integrated circuit (ROIC). The array is monolithically developed on the ROIC, which is fabricated using a 130 nm CMOS process and features a standard

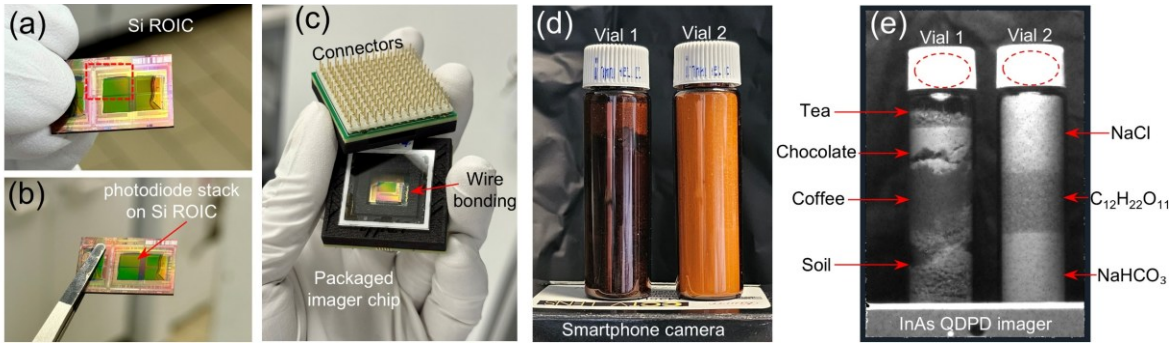


Figure 6. (a)−(b) Fabricated InAs photodiode on Si ROIC, (c) packaged and wire bonded thin film InAs infrared imager chip, and (d)−(e) sample pictures taken by smartphone and InAs imager comparing the infrared imaging capability.

3-transistor (3T) pixel architecture with a 5 μm pixel pitch. The final array consists of 512×768 pixels, with illumination incident through the top ITO contact. Photo-generated carriers are collected at the bottom electrode and read out via charge integration in the ROIC in-pixel capacitor. Demonstration images are taken under halogen lamp at −3 V and 37.5 μs integration time.

Figure 6a–b show the fabricated InAs QDPD array monolithically integrated on the Si ROIC, and Figure 6c displays the packaged and wire-bonded complete imager chip. To highlight the infrared imaging capability of our thin film InAs QDPD imager, we prepare two dark brown vials filled with various common materials. Vial 1 contains tea, chocolate, coffee and soil while vial 2 contains table salt (NaCl), sugar ($C_{12}H_{22}O_{11}$) and sodium bicarbonate ($NaHCO_3$). As shown in Figure 6d, a reference image taken with a smartphone camera reveals minimal contrast through Vial 1 due to the absorption of visible light by the brown glass. In contrast, the InAs QDPD imager (Figure 6e) clearly distinguishes between the contents of Vial 1, enabled by material-specific reflection and absorption features at 1200 nm. Similarly, for Vial 2, where the powders appear nearly identical under visible light, the QDPD imager successfully resolves differences between the contents. Notably, the plastic vial caps appear extremely bright in the infrared image due to

strong reflection of 1200 nm light, which overwhelms the contrast and makes the “imec” label no longer visible.

3. CONCLUSIONS

We present a thin-film InAs colloidal quantum dot photodiode that achieves low dark current, efficient infrared detection at 1200 nm, and successful monolithic integration with CMOS ROIC. Through temperature-dependent J−V, C−V, and C−f spectroscopy, we identify thermally activated transport and extract the trap states below the conduction band: a continuum of shallow tail states, that lead to the deep trap states at 0.36 ± 0.05 eV. We reveal their role in carrier generation and noise. The photodiode enables infrared imaging at 1200 nm, with strong material-specific contrast beyond the visible range. Our comprehensive analysis from device stack design to dark carrier dynamics highlights the need for improved passivation strategies and optimized junction engineering to further enhance device performance. These findings advance the understanding of trap-limited carrier dynamics in QDPDs and offer a scalable path toward high-resolution, CMOS-compatible NIR and SWIR imaging technologies.

4. EXPERIMENT

The InAs (λ = 1200 nm) colloidal quantum dots capped with oleic acid were purchased from Quantum Solutions ® in n-octane. Ligand exchange was performed under a nitrogen atmosphere using a solution-phase $InBr_3$ treatment following the method introduced by Sargent et al. [12,17]. Briefly, the indium (III) bromide ($InBr_3$) and ammonium acetate ligands were dissolved in DMF, mixed and filtered. The CQDs in n-octane were then gradually added to the ligand solution,

vortexed, and centrifuged to transfer the nanocrystals into the DMF phase. This phase transfer step was repeated 3–4 times, replacing the discarded top n-octane layer each time with fresh solvent. The CQDs were precipitated using anhydrous toluene and finally redispersed in DMF and filtered for device fabrication. The chemical binding energies of the ligand-exchanged CQDs are included in Figure S10.

For the QDPD, first, a silicon substrate with a pre-patterned TiN bottom electrode was cleaned in an ultrasonic bath with acetone and isopropyl alcohol. Then, IGZO was sputtered from a target with In:Ga:Zn ratio of 1:1:1 and subsequently patterned by photolithography to form islands. The active layer InAs-$InBr_3$ was spin coated in 2 steps and annealed at 150 ºC to remove any residual solvent. For the hole transport layers, the CuI layer was deposited by thermal evaporation followed by spin coating of PTB7-Th. Finally, the device was completed with MoOx and the transparent top electrode ITO which were deposited by thermal evaporation and sputtering, respectively.

The thin-film QDPD imager was fabricated by monolithically integrating the InAs photodiode stack onto a custom-designed ROIC manufactured in a 130 nm CMOS process. The chip contains an array of 768 × 512 pixels, each with a 5 μm pitch and a 3-transistor (3T) pixel readout architecture. The pixel outputs are buffered and serially multiplexed on-chip, followed by digitization through an integrated 16-bit analog-to-digital converter (ADC). Further details on the ROIC design are provided in our earlier reports [3,37]. Device processing was carried out directly at the chip level using the same thin-film fabrication flow. The completed sensor was then wire bonded to a printed circuit board, packaged, and had a lens attached for imaging, as illustrated in Figure S14.

The X-ray and ultraviolet photoelectron spectroscopy (XPS and UPS) measurements were performed using a VersaProbe III instrument from Physical Electronics. The tool is equipped with monochromatized Al K-alpha (1486.6 eV) and He I (21.2 eV) UV radiation for XPS and UPS sources, respectively. The XPS spectra was acquired by 100×100 μm^2 X-ray beam spot size with the flood gun on while the UPS spectra were recorded by a ~1 mm^2 UV beam. During UPS measurements, a sample bias of −5 V was applied during all the measurements to detect the secondary electron (SE) emission edge. All post-processing of XPS and UPS spectra was performed using MultiPak (data reduction software for XPS and AES by ULVAC-PHI).

The transmission electron microscopy (TEM) images were taken by scanning transmission electron microscope (STEM) FEI Titan3™ G2 60-300 S/TEM at 200 KV. The optical absorption spectra were acquired on a UV-3600i Plus spectrophotometer from Shimadzu Corporation, Japan.

The dark J−V characteristics were measured with Keithley 2602B System. The EQE spectra were acquired using a Stanford SR830 lock-in amplifier coupled with a monochromator and a 145 W halogen lamp, using a calibrated Ge photodiode as the spectral reference. The transient and steady-state photo response along with transient photovoltage decay measurements were conducted using the Paios System (Fluxim AG, Switzerland). The noise current spectral density was measured using Keysight E4727B Advanced Low-Frequency Noise Analyzer and Keysight B1500 parameter analyzer. Temperature-dependent dark J−V, C−V, and C−f measurements were carried out using a Keysight B1500 parameter analyzer and an Agilent E4980A precision LCR meter, respectively, coupled with a cryostat from Lake Shore Cryotronics, Inc.

ASSOCIATED CONTENT

Supporting Information

Normalized absorptance spectra, HR-TEM images, ligand exchange process schematic, elemental mapping and depth profile, uniformity and aging effects, transient photocurrent response, Poole-Frenkel plot, capacitance–frequency spectra, XPS narrow band spectra, normalized transient photovoltage decay, space charge limited current analysis, infrared camera setup

AUTHOR INFORMATION

Corresponding Authors

Abu Bakar Siddik- IMEC, Kapeldreef 75, 3001 Leuven, Belgium, and Department of Electrical Engineering ESAT, KU Leuven, Kasteelpark Arenberg 10, 3001 Leuven, Belgium.

abu.bakar.siddik@imec.be

Epimitheas Georgitzikis- IMEC, Kapeldreef 75, 3001 Leuven, Belgium.

epimitheas.georgitzikis@imec.be

Author Contributions

The manuscript was written through contributions of all authors. All authors have given approval to the final version of the manuscript.

Notes

The authors declare no competing financial interest.

ACKNOWLEDGMENT

REFERENCES

(1) Pejović, V.; Georgitzikis, E.; Lieberman, I.; Malinowski, P. E.; Heremans, P.; Cheyns, D. Photodetectors Based on Lead Sulfide Quantum Dot and Organic Absorbers for Multispectral Sensing in the Visible to Short-Wave Infrared Range. *Adv Funct Materials* **2022**, *32* (28), 2201424. https://doi.org/10.1002/adfm.202201424.
(2) Leemans, J.; Pejović, V.; Georgitzikis, E.; Minjauw, M.; Siddik, A. B.; Deng, Y.; Kuang, Y.; Roelkens, G.; Detavernier, C.; Lieberman, I.; Malinowski, P. E.; Cheyns, D.; Hens, Z. Colloidal III–V Quantum Dot Photodiodes for Short-Wave Infrared Photodetection. *Advanced Science* **2022**, *9* (17), 2200844. https://doi.org/10.1002/advs.202200844.
(3) Pejovic, V.; Georgitzikis, E.; Lee, J.; Lieberman, I.; Cheyns, D.; Heremans, P.; Malinowski, P. E. Infrared Colloidal Quantum Dot Image Sensors. *IEEE Trans. Electron Devices* **2022**, *69* (6), 2840–2850. https://doi.org/10.1109/TED.2021.3133191.
(4) Kagawa, Y.; Kamibayashi, T.; Yamano, Y.; Nishio, K.; Sakamoto, A.; Yamada, T.; Shimizu, K.; Hirano, T.; Iwamoto, H. Development of Face-to-Face and Face-to-Back Ultra-Fine Pitch Cu-Cu Hybrid Bonding. In *2022 IEEE 72nd Electronic Components and Technology Conference (ECTC)*; IEEE: San Diego, CA, USA, 2022; pp 306–311. https://doi.org/10.1109/ECTC51906.2022.00057.
(5) Kagawa, Y.; Kamibayashi, T.; Fujii, N.; Furuse, S.; Yamada, T.; Hirano, T.; Iwamoto, H. Cu-Cu Wiring: The Novel Structure of Cu-Cu Hybrid Bonding. In *2023 IEEE 73rd Electronic Components and Technology Conference (ECTC)*; IEEE: Orlando, FL, USA, 2023; pp 103–108. https://doi.org/10.1109/ECTC51909.2023.00026.
(6) Xia, P.; Zhu, T.; Imran, M.; Pina, J. M.; Atan, O.; Najarian, A. M.; Chen, H.; Zhang, Y.; Jung, E.; Biondi, M.; Vafaie, M.; Li, C.; Grater, L.; Khatri, A.; Singh, A.; Hoogland, S.; Sargent, E. H. Arresting Ion Migration from the ETL Increases Stability in Infrared Light Detectors Based on III-V Colloidal Quantum Dots. *Advanced Materials* **2024**, *36* (4), 2310122. https://doi.org/10.1002/adma.202310122.
(7) Song, J. H.; Choi, H.; Pham, H. T.; Jeong, S. Energy Level Tuned Indium Arsenide Colloidal Quantum Dot Films for Efficient Photovoltaics. *Nat Commun* **2018**, *9* (1), 4267. https://doi.org/10.1038/s41467-018-06399-4.
(8) Siddik, A. B.; Georgitzikis, E.; Song, W.; Papadopoulou, A.; Zaman, A. U.; Lim, M. J.; Pejovic, V.; Lieberman, I.; Malinowski, P. E.; Genoe, J.; Conard, T.; Cheyns, D.; Heremans, P. PbS and InAs Quantum-Dot Thin Films for Short-Wave Infrared Detectors. *ACS Appl. Nano Mater.* **2024**, *7* (22), 25412–25422. https://doi.org/10.1021/acsanm.4c04386.
(9) Shin, D.; Jeong, H.; Kim, J.; Jang, E.; Park, Y.; Jeong, S. High Performance Infrared InAs Colloidal Quantum Dot Photodetector with 79% EQE Enabled by an Extended Absorber Layer. *Advanced Optical Materials* **2025**, *13* (1), 2401931. https://doi.org/10.1002/adom.202401931.
(10) Jung, B. K.; Yoo, H.; Seo, B.; Choi, H. J.; Choi, Y. K.; Kim, T. H.; Oh, N.; Kim, S. Y.; Kim, S.; Lee, Y.; Shim, J. W.; Park, H. Y.; Hwang, G. W.; Ng, T. N.; Oh, S. J. High-Affinity Ligand-Enhanced Passivation of Group III–V Colloidal Quantum Dots for Sensitive Near-Infrared Photodetection. *ACS Energy Lett.* **2024**, *9* (2), 504–512. https://doi.org/10.1021/acsenergylett.3c02515.
(11) Xia, P.; Wang, S.; Chen, Y.; Gulsaran, A.; Zhang, Y.; Vafaie, M.; Imran, M.; Najarian, A. M.; Liu, Y.; Ban, H.; Sagar, L. K.; Yavuz, M.; Sargent, E. H. Improved Facet and Edge Passivation in Near-Infrared III-V Colloidal Quantum Dot Photodetectors. *Advanced Materials* **2025**, *37* (18), 2419020. https://doi.org/10.1002/adma.202419020.

(12) Vafaie, M.; Morteza Najarian, A.; Xu, J.; Richter, L. J.; Li, R.; Zhang, Y.; Imran, M.; Xia, P.; Ban, H. W.; Levina, L.; Singh, A.; Meitzner, J.; Pattantyus-Abraham, A. G.; García De Arquer, F. P.; Sargent, E. H. Molecular Surface Programming of Rectifying Junctions between InAs Colloidal Quantum Dot Solids. *Proc. Natl. Acad. Sci. U.S.A.* **2023**, *120* (41), e2305327120. https://doi.org/10.1073/pnas.2305327120.

(13) Kim, S.; Yeon, S.; Lee, M.; Jin, J.; Shin, S.; Gwak, N.; Jeong, I.; Jang, H.; Hwang, G. W.; Oh, N. Chemically and Electronically Active Metal Ions on InAs Quantum Dots for Infrared Detectors. *NPG Asia Mater* **2023**, *15* (1), 30. https://doi.org/10.1038/s41427-023-00477-w.

(14) Sheikh, T.; Mir, W. J.; Alofi, A.; Skoroterski, M.; Zhou, R.; Nematulloev, S.; Hedhili, M. N.; Hassine, M. B.; Khan, M. S.; Yorov, K. E.; Hasanov, B. E.; Liao, H.; Yang, Y.; Shamim, A.; Abulikemu, M.; Mohammed, O. F.; Bakr, O. M. Surface-Reconstructed InAs Colloidal Nanorod Quantum Dots for Efficient Deep-Shortwave Infrared Emission and Photodetection. *J. Am. Chem. Soc.* **2024**, *146* (42), 29094–29103. https://doi.org/10.1021/jacs.4c10755.

(15) Ban, H. W.; Vafaie, M.; Levina, L.; Xia, P.; Imran, M.; Liu, Y.; Najarian, A. M.; Sargent, E. H. Resurfacing of InAs Colloidal Quantum Dots Equalizes Photodetector Performance across Synthetic Routes. *J. Am. Chem. Soc.* **2024**, *146* (36), 24935–24944. https://doi.org/10.1021/jacs.4c06202.

(16) Xia, P.; Wang, S.; Chen, Y.; Gulsaran, A.; Zhang, Y.; Vafaie, M.; Imran, M.; Najarian, A. M.; Liu, Y.; Ban, H.; Sagar, L. K.; Yavuz, M.; Sargent, E. H. Improved Facet and Edge Passivation in Near-Infrared III-V Colloidal Quantum Dot Photodetectors. *Advanced Materials* **2025**, *37* (18), 2419020. https://doi.org/10.1002/adma.202419020.

(17) Xia, P.; Sun, B.; Biondi, M.; Xu, J.; Atan, O.; Imran, M.; Hassan, Y.; Liu, Y.; Pina, J. M.; Najarian, A. M.; Grater, L.; Bertens, K.; Sagar, L. K.; Anwar, H.; Choi, M.; Zhang, Y.; Hasham, M.; García de Arquer, F. P.; Hoogland, S.; Wilson, M. W. B.; Sargent, E. H. Sequential Co-Passivation in InAs Colloidal Quantum Dot Solids Enables Efficient Near-Infrared Photodetectors. *Advanced Materials* **2023**, *35* (28), 2301842. https://doi.org/10.1002/adma.202301842.

(18) Lee, J.; Georgitzikis, E.; Hermans, Y.; Papadopoulos, N.; Chandrasekaran, N.; Jin, M.; Siddik, A. B.; De Roose, F.; Uytterhoeven, G.; Kim, J. H.; Puybaret, R.; Li, Y.; Pejovic, V.; Karve, G.; Cheyns, D.; Genoe, J.; Malinowski, P. E.; Heremans, P.; Myny, K. Thin-Film Image Sensors with a Pinned Photodiode Structure. *Nat Electron* **2023**, *6* (8), 590–598. https://doi.org/10.1038/s41928-023-01016-9.

(19) Srivastava, R. P.; Jung, H.-S.; Khang, D.-Y. Transfer-Printed Cuprous Iodide (CuI) Hole Transporting Layer for Low Temperature Processed Perovskite Solar Cells. *Nanomaterials* **2022**, *12* (9), 1467. https://doi.org/10.3390/nano12091467.

(20) Yang, Z.; Wang, M.; Shukla, S.; Zhu, Y.; Deng, J.; Ge, H.; Wang, X.; Xiong, Q. Developing Seedless Growth of ZnO Micro/Nanowire Arrays towards ZnO/FeS2/CuI P-I-N Photodiode Application. *Sci Rep* **2015**, *5* (1), 11377. https://doi.org/10.1038/srep11377.

(21) Sheikh, T.; Mir, W. J.; Nematulloev, S.; Maity, P.; Yorov, K. E.; Hedhili, M. N.; Emwas, A.-H.; Khan, M. S.; Abulikemu, M.; Mohammed, O. F.; Bakr, O. M. InAs Nanorod Colloidal Quantum Dots with Tunable Bandgaps Deep into the Short-Wave Infrared. *ACS Nano* **2023**, *17* (22), 23094–23102. https://doi.org/10.1021/acsnano.3c08796.

(22) Franke, D.; Harris, D. K.; Chen, O.; Bruns, O. T.; Carr, J. A.; Wilson, M. W. B.; Bawendi, M. G. Continuous Injection Synthesis of Indium Arsenide Quantum Dots Emissive in the Short-Wavelength Infrared. *Nat Commun* **2016**, *7* (1), 12749. https://doi.org/10.1038/ncomms12749.

(23) Lee, J.; Zhao, T.; Yang, S.; Muduli, M.; Murray, C. B.; Kagan, C. R. One-Pot Heat-up Synthesis of Short-Wavelength Infrared, Colloidal InAs Quantum Dots. *The Journal of Chemical Physics* **2024**, *160* (7), 071103. https://doi.org/10.1063/5.0187162.
(24) Siddik, A. B.; Georgitzikis, E.; Hermans, Y.; Kang, J.; Kim, J. H.; Pejovic, V.; Lieberman, I.; Malinowski, P. E.; Kadashchuk, A.; Genoe, J.; Conard, T.; Cheyns, D.; Heremans, P. Interface-Engineered Organic Near-Infrared Photodetector for Imaging Applications. *ACS Appl. Mater. Interfaces* **2023**, *15* (25), 30534–30542. https://doi.org/10.1021/acsami.3c03708.
(25) Vafaie, M.; Morteza Najarian, A.; Xu, J.; Richter, L. J.; Li, R.; Zhang, Y.; Imran, M.; Xia, P.; Ban, H. W.; Levina, L.; Singh, A.; Meitzner, J.; Pattantyus-Abraham, A. G.; García de Arquer, F. P.; Sargent, E. H. Molecular Surface Programming of Rectifying Junctions between InAs Colloidal Quantum Dot Solids. *Proc. Natl. Acad. Sci. U.S.A.* **2023**, *120* (41), e2305327120. https://doi.org/10.1073/pnas.2305327120.
(26) Konstantatos, G.; Clifford, J.; Levina, L.; Sargent, E. H. Sensitive Solution-Processed Visible-Wavelength Photodetectors. *Nature Photon* **2007**, *1* (9), 531–534. https://doi.org/10.1038/nphoton.2007.147.
(27) Konstantatos, G.; Howard, I.; Fischer, A.; Hoogland, S.; Clifford, J.; Klem, E.; Levina, L.; Sargent, E. H. Ultrasensitive Solution-Cast Quantum Dot Photodetectors. *Nature* **2006**, *442* (7099), 180–183. https://doi.org/10.1038/nature04855.
(28) Fang, Y.; Armin, A.; Meredith, P.; Huang, J. Accurate Characterization of Next-Generation Thin-Film Photodetectors. *Nature Photon* **2019**, *13* (1), 1–4. https://doi.org/10.1038/s41566-018-0288-z.
(29) Xu, M.; Chen, D.; Lin, J.; Lu, X.; Deng, Y.; He, S.; Zhu, X.; Jin, W.; Jin, Y. Quantum-Dot Light-Emitting Diodes with Fermi-Level Pinning at the Hole-Injection/Hole-Transporting Interfaces. *Nano Res.* **2022**, *15* (8), 7453–7459. https://doi.org/10.1007/s12274-022-4260-3.
(30) Akaike, K.; Koch, N.; Oehzelt, M. Fermi Level Pinning Induced Electrostatic Fields and Band Bending at Organic Heterojunctions. *Applied Physics Letters* **2014**, *105* (22), 223303. https://doi.org/10.1063/1.4903360.
(31) Amsalem, P.; Niederhausen, J.; Wilke, A.; Heimel, G.; Schlesinger, R.; Winkler, S.; Vollmer, A.; Rabe, J. P.; Koch, N. Role of Charge Transfer, Dipole-Dipole Interactions, and Electrostatics in Fermi-Level Pinning at a Molecular Heterojunction on a Metal Surface. *Phys. Rev. B* **2013**, *87* (3), 035440. https://doi.org/10.1103/PhysRevB.87.035440.
(32) Sun, B.; Najarian, A. M.; Zheng, C.; Sagar, L.; Choi, M.-J.; Li, X.; Levina, L.; Baek, S.-W.; Lee, S.; Kirmani, A. R.; Abed, J.; Liu, M.; Li, P.; Richter, L.; Voznyy, O.; Lu, Z.-H.; Arquer, F. P. G. D.; Sargent, E. Sub-Nanosecond Infrared Photodetection Using III-V Colloidal Quantum Dots. November 20, 2020. https://doi.org/10.21203/rs.3.rs-92318/v1.
(33) Walter, T.; Herberholz, R.; Müller, C.; Schock, H. W. Determination of Defect Distributions from Admittance Measurements and Application to Cu(In,Ga)Se2 Based Heterojunctions. *Journal of Applied Physics* **1996**, *80* (8), 4411–4420. https://doi.org/10.1063/1.363401.
(34) Kublitski, J.; Hofacker, A.; Boroujeni, B. K.; Benduhn, J.; Nikolis, V. C.; Kaiser, C.; Spoltore, D.; Kleemann, H.; Fischer, A.; Ellinger, F.; Vandewal, K.; Leo, K. Reverse Dark Current in Organic Photodetectors and the Major Role of Traps as Source of Noise. *Nat Commun* **2021**, *12* (1), 551. https://doi.org/10.1038/s41467-020-20856-z.
(35) Kwan Kim, J.; Hoon Song, J.; Choi, H.; Jae Baik, S.; Jeong, S. Space Charge Limited Conduction in Ultrathin PbS Quantum Dot Solid Diodes. *Journal of Applied Physics* **2014**, *115* (5). https://doi.org/10.1063/1.4863725.

(36) Kim, K. M.; Choi, B. J.; Shin, Y. C.; Choi, S.; Hwang, C. S. Anode-Interface Localized Filamentary Mechanism in Resistive Switching of TiO2 Thin Films. *Applied Physics Letters* **2007**, *91* (1). https://doi.org/10.1063/1.2749846.

(37) Pejovic, V.; Lee, J.; Georgitzikis, E.; Li, Y.; Kim, J. H.; Lieberman, I.; Malinowski, P. E.; Heremans, P.; Cheyns, D. Thin-Film Photodetector Optimization for High-Performance Short-Wavelength Infrared Imaging. *IEEE Electron Device Lett.* **2021**, *42* (8), 1196–1199. https://doi.org/10.1109/LED.2021.3093081.

